CHEMISTRY OF MATERIALS

pubs.acs.org/cm

Article

Tunable Electrical Conductivity of Flexible Metal−Organic Frameworks

Sanggyu Chong,[§] Sven M. J. Rogge,[§] and Jihan Kim*

Cite This: https://doi.org/10.1021/acs.chemmater.1c03236

Read Online

ACCESS | Metrics & More | Article Recommendations | Supporting Information

ABSTRACT: We present the computational design of naphthalene diimide (NDI)-containing metal pyrazolate metal−organic frameworks (MOFs) [M(NDIDP), M = Zn, Co, and Fe] judiciously bestowed with both framework flexibility and electrical conductivity. M(NDIDP) MOFs exhibit "wine rack" type flexibility, allowing them to partake in pressure-induced structural transitions at low pressures and room temperature. The MOFs are also equipped with closely packed redox-active NDI moieties, which results in dispersive conduction band minima for efficient charge transport and conductivity. Remarkably, structural transitions of the designed MOFs are found to facilitate the rearrangement of NDI moieties. As a result, charge transport properties of M(NDIDP) MOFs can be finely tuned, which is evidenced by the gradual shift from one-dimensional to two-dimensional charge transport and up to 7.5-fold reduction in carrier effective mass ($2.76m_0$−$0.37m_0$) when transitioning between different structural configurations. The unprecedented discovery of flexible MOFs with tunable electrical conductivity arising from configuration-dependent charge transport behavior firmly establishes MOFs as versatile candidate materials for multifunctional electronics.

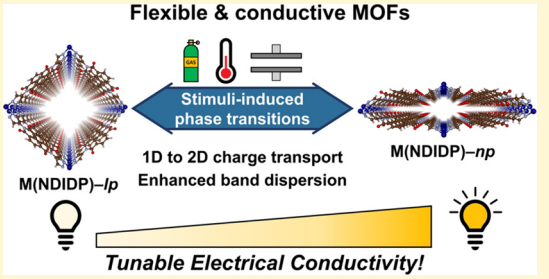

INTRODUCTION

The high modularity of metal−organic frameworks (MOFs) with multiple design parameters (e.g., metal ions/clusters,[1] organic linkers,[2] topologies,[3] and defects[4,5]) has led to the discovery of a large number of MOFs with a wide range of properties and functionalities. Judicious choice of the framework components makes it possible to tailor these materials for a variety of applications, ranging from gas storage and separation[6] to catalysis,[7] drug delivery,[8] water harvesting,[9,10] and so forth. More recently, research has shown that electrical conductivity can be induced in MOFs.[11−15] Because of their porosity and conventional use of electrically inactive components (i.e., closed-shell metals and σ-bridged organic linkers), MOFs have long been considered as electrical insulators. However, by synthesizing MOFs from redox-active metals and linkers that allow significant delocalization of charge carriers, it becomes possible to secure long-range charge transport (CT) pathways in MOFs to induce conductivity. Experimental conductivities of MOFs have reached up to 2500 S/cm,[16−18] and as such, they have been successfully integrated in field-effect transistors,[19] supercapacitors,[20] chemiresistive sensors,[21−23] and electrocatalysts.[24] While substantial progress has been made, research thus far has mainly focused on inducing the conductivity in MOFs. To make further breakthroughs, however, focus should be shifted toward synergistically combining conductivity with other properties unique to MOFs, allowing novel application schemes unfeasible in other materials.

One of the most intriguing properties of MOFs that differentiates them from other materials is framework flexibility.[25] Generally, MOFs are considered to be more flexible than other solid crystalline materials as they inherently possess several structural degrees of freedom (e.g., linker rotation and lattice deformation). Here, however, we specifically refer to flexibility as those cases where MOF constituents participate in large-amplitude structural transitions, whilst conserving the original framework topology. Such flexible MOFs are capable of undergoing significant expansion or contraction of the framework, which can drastically alter their pore geometry and internal arrangement of framework components. This can be viewed akin to a switch or a dial, as the framework is able to effectively transition between clearly distinct states or structural configurations via external stimuli (e.g., guest adsorption, temperature, light, and pressure).[26,27] As such, framework flexibility can effectively instill new external parameters (e.g., stimuli and time) for the control of MOF properties, opening up many new applications.[28] Previous studies have utilized the flexibility of MOFs for selective chemical sensing,[29] switchable catalysis,[30] or band gap

Received: September 18, 2021
Revised: December 19, 2021

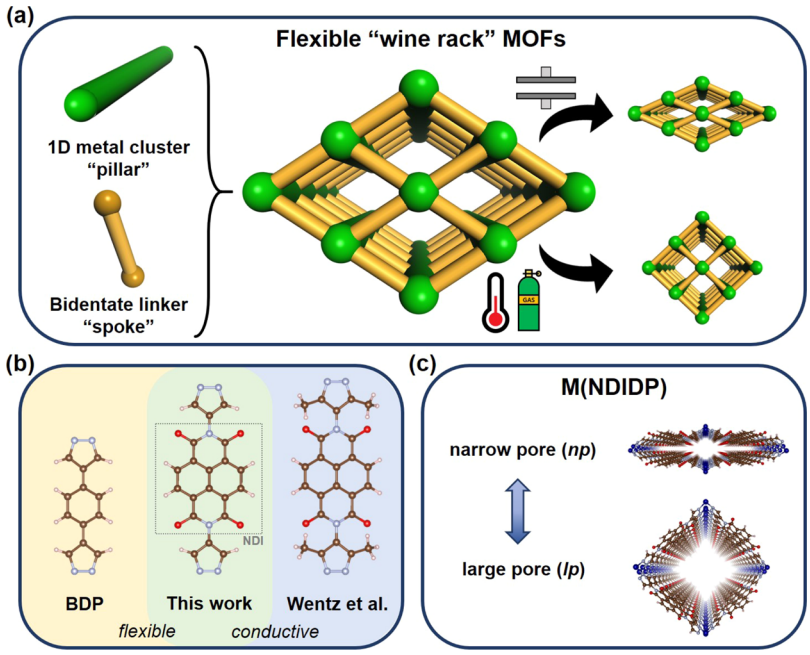

Figure 1. (a) Flexible MOFs with wine rack structural motif built from 1D metal clusters and bidentate organic linkers. (b) Bidentate pyrazolate linkers considered for MOF construction. (c) Structure of the newly proposed M(NDIDP) MOFs shown along with the metals that have been used for the construction of the three separate MOFs.

modulation.[31] However, to the best of our knowledge, no one has linked framework flexibility directly with the electrical conductivity of MOFs, which could potentially lead to tunable electrical conduction properties.

In this computational study, we have performed the modular design of MOFs that simultaneously harness both framework flexibility and electrical conductivity. To demonstrate the possibility of inducing electrical conductivity in MOFs exhibiting framework flexibility, a well-known flexible MOF [i.e., M(BDP),[32−34] H_2BDP = 1,4-di(1H-pyrazol-4-yl)-benzene] was adopted as the template framework. Then, central benzene groups of the linkers were replaced with redox-active 1,4,5,8-naphthalene diimide (NDI) moieties, well-known charge acceptors,[35−37] resulting in the newly proposed MOFs referred to as M(NDIDP). Density functional theory (DFT) modeling of M(NDIDP) MOFs was performed to discover the presence of multiple metastable phases with vastly different internal arrangement of the NDI moieties. Next, molecular dynamics (MD) simulations with DFT-derived force fields were carried out to show that the MOFs can undergo pressure-induced phase transitions at room temperature, firmly establishing their framework flexibility. DFT electronic band structure analysis revealed that M(NDIDP) MOFs exhibit notable dispersions in the conduction band minima for efficient charge transport and conductivity. Strikingly, charge transport properties of M(NDIDP) were found to be highly configuration-dependent, as evidenced by the shift from one-dimensional (1D) to two-dimensional (2D) charge transport and up to 5.7-fold increase in band dispersion (7.5-fold reduction in carrier effective mass) between different structural configurations within a single material. Such configuration-dependent charge transport behavior effectively demonstrates that electrical conductivity of M(NDIDP) MOFs can be finely tuned via the application of external stimuli, making them excellent candidate materials for multifunctional electronics.

METHODS

DFT Calculations. Kohn−Sham density functional theory (DFT) calculations were performed to obtain the optimized configurations of each of the M(NDIDP) MOFs and analyze the resulting electronic structures. All DFT calculations in this work were carried out with the Vienna ab initio simulation package (VASP).[38−40] The projector augmented wave (PAW) method[41,42] was used to describe the interactions between the ions and electrons. The exchange-correlation term was described within the generalized gradient approximation (GGA) using the Perdew−Burke−Ernzerhof (PBE) functional.[43] In the newly designed MOFs, it is important to accurately account for the van der Waals interactions between the NDI moieties, given their high degree of aromaticity. Hence, DFT-D3 dispersion corrections with Becke−Johnson damping were employed.[44] Γ-centered k-point grids with spacings less than 0.3 $Å^{-1}$ were used in the calculations. The kinetic energy cutoff was set at 600 eV, and the self-consistent field (SCF) convergence criterion was fixed at 1×10^{-6} eV. Gaussian smearing was performed with a sigma value of 0.01 Å. Given the presence of unpaired d-orbital electrons, spin polarization was considered for Co(NDIDP) and Fe(NDIDP). High-spin ferromagnetic ordering along each 1D metal cluster was observed to be the most stable and hence used to report the system energies.

Geometry optimizations were performed to construct the $E(V)$ profiles of each material. In each optimization, a volume constraint was applied. That is, the total volume of the unit cell was fixed, but the internal atomic coordinates and the lattice parameters were relaxed until the energy minimum was found. Relaxation was continued until the Hellmann−Feynman forces became lower than 0.01 eV/Å for all the atoms. After successfully optimizing the MOF at a given volume, the length of the lattice parameter a was incrementally increased or decreased to provide the starting configuration for the adjacent volume point. This procedure was repeated until the entire volume range of interest was covered. Electronic band structures were subsequently calculated for the configurations of interest. While the PBE functional can provide an accurate description of the structure of these materials, it is known to underestimate the band gaps of semiconducting materials. Hence, the HSE06 hybrid functional[45] was used to more accurately describe the band structures. In doing so, revised D3 damping parameters for HSE06 reported by Moellmann and Grimme were used.[46] Ten equidistant k-points within the first

https://doi.org/10.1021/acs.chemmater.1c03236
Chem. Mater. XXXX, XXX, XXX−XXX

Brillouin zone were sampled along the high symmetry paths of interest, that is, the $\Gamma-X$ and $\Gamma-Z$ paths. Carrier effective masses were calculated with the sumo package,[47] using a least-squares fit with five sample points and assuming nonparabolicity of the bands.

MD Simulations. Force field-based MD simulations were performed to study the pressure-induced structural transitions of M(NDIDP). To this end, for each of the DFT-optimized structures, first, the Hessian matrix was calculated with VASP using 0.015 Å displacements and an SCF convergence criterium of 1×10^{-8} eV for improved accuracy. The ab initio periodic Hessian and optimized structure was then taken as inputs to the QuickFF software[48,49] to derive the covalent force field parameters for interactions, including cross-terms and using the force field atom types provided in Figure S19. Gaussian-like atomic charges were used to describe the electrostatic interactions and were determined using the minimal basis iterative stockholder (MBIS) partitioning scheme, as implemented in HORTON.[50] To this end, GPAW calculations[51,52] were performed on the optimized geometries to obtain the all-electron density necessary for the MBIS scheme. The radii of the Gaussian charges were obtained by following the fitting approach suggested by Chen and Martínez.[53] Finally, the MM3 Buckingham potential[54] was used to account for the van der Waals interactions.

Using these force fields, MD simulations were performed in Yaff for a variety of volumes to obtain the $P(V)$ equations of state.[55] Simulations were conducted for $1 \times 1 \times 2$ supercells of the M(NDIDP) MOFs in the $(N, V, \sigma_a = 0, T)$ ensemble, where σ_a refers to the deviatoric stress component of the stress tensor.[56] In this ensemble, the unit cell V is constrained, but the simulation cell shape can fluctuate freely. From these simulations, the average pressure the material exerts on its environment is extracted. This average pressure equals the external pressure exerted on the material in the mechanical equilibrium and can thus be used to construct the macroscopic pressure-versus-volume equations of state. A Nosé−Hoover chain thermostat[57,58] with a chain length of 3 and a 0.1 ps relaxation time was used to control the system temperature. σ_a was controlled using the Martyna−Tobias−Tuckerman−Klein barostat[59] with a 1 ps relaxation time. The velocity Verlet integration algorithm was used with a timestep of 0.5 fs to solve the equations of motion. A distance cutoff of 15 Å was used for the van der Waals interactions with a smooth cutoff. For the electrostatic interactions, an Ewald summation was performed with a real-space cutoff of 15 Å, a splitting parameter of 0.213 $Å^{-1}$, and a reciprocal space cutoff of 0.32 $Å^{-1}$. Each simulation consisted of a 0.5 ns equilibration run, followed by a 0.5 ns production run. The obtained $P(V)$ equations of state were locally smoothened using the Savitzky−Golay filter.[60]

RESULTS AND DISCUSSION

Modular Design of M(NDIDP). Many flexible MOFs have been synthesized to date, and diverse structural motifs for framework flexibility have been implemented. One of the most common structural motifs for flexibility is the "wine rack" motif, where 1D metal clusters are present as pillars and bidentate linkers serve as spokes that bind the pillars together (Figure 1a). In such MOFs, coordination bonds between the metals and linkers function as hinges, and they are collectively arranged in a manner that allows for a significant expansion and contraction of the framework. Representative MOFs of this motif are MIL-47,[61] MIL-53,[62] and M(BDP),[32−34] which are widely recognized for their stepwise gas adsorption behavior arising from the large variability in the pore volume. Here, it is important to note that flexibility in these MOFs is conferred by their unique metal-linker coordination environment and topologies. Hence, by performing further structural modifications without altering the coordination environment, new properties could be instilled in the wine rack MOFs whilst retaining their flexibility.

Recently, Wentz et al. reported switchable electrical conductivity in a zinc pyrazolate MOF (Zn-NDI) via reversible n-doping of the framework.[63] Interestingly, this MOF is isoreticular to M(BDP), but displays two key structural differences: redox-active NDI moieties are present as central moieties in the linkers and the pyrazolate binding moieties are methylated at the 3 and 5 positions (Figure 1b). Electrical conductivity is effectively conferred to the MOF by the presence of NDI moieties, as they are stacked together in a regular fashion to facilitate CT. However, the methyl groups of pyrazolate binding moieties are found to significantly hinder the MOF from partaking in large-amplitude structural transitions despite the wine rack motif (see the Supporting Information). As such, we conjectured that modular substitution of the methyl groups with hydrogens, or conversely, benzene in M(BDP) with NDI moieties, could induce electrical conductivity in the resulting MOF while retaining the framework flexibility, thereby allowing for stimuli-controlled conductivity.

The resultant MOFs were constructed in silico (Figure 1c). First, a four-linker unit cell of M(BDP) was procured from the Cambridge Structural Database (refcode: QUPZAE and QUPZIM). The central benzene moieties of the BDP linkers were then computationally substituted with NDI, resulting in the proposed MOF structures. In the process, the original unit cell of M(BDP) was expanded along the linker directions to easily accommodate the redox-active NDI moieties. Note that this process is effectively equivalent to the substitution of methyl groups on the pyrazolate groups of Zn-NDI with hydrogens. Three different MOFs were built from Zn, Co, and Fe metal pillars, which allows further investigation of how different metal ions affect the resulting properties. The new MOFs are herein referred to as M(NDIDP) (M = Zn, Co, and Fe, NDIDP = *N*,*N*-di(1H-pyrazol-4-yl)-1,4,5,8-naphthalenediimide). It must be stated that the NDI-containing linkers incorporated into M(NDIDP) are yet to be synthesized. Nonetheless, judging from the abundance of similar NDI-containing organic linkers and their successful incorporation into MOFs,[64−68] we expect the linker synthesis to become possible in the near future.

Flexibility of M(NDIDP): Energy vs Volume Profile. Next, calculations were performed to determine whether framework flexibility was successfully manifested in our M(NDIDP) MOFs. As previously discussed, flexibility targeted in this work is characterized by large-amplitude expansion and contraction of the framework. In such a case, structural degrees of freedom exhibited by the MOF would allow a wide range of energetically accessible configurations, often with multiple metastable phases present as minima in the (free) energy profile. Conversely, a rigid MOF would be characterized by a narrow, parabolic energy profile with a single global minimum. Note that the expansion and contraction of flexible MOFs often incur vast differences in their unit cell volume. Hence, energy-versus-volume or $E(V)$ profiles for each of the M(NDIDP) MOFs were obtained at the DFT level of theory (see Figure 2). Here, each point corresponds to an optimized structural configuration at the given unit cell volume, plotted according to its energy difference from the global energy minimum. The $E(V)$ profiles of all three M(NDIDP) MOFs exhibit a significantly wide range of energetically accessible configurations (i.e., $\Delta E < 2$ eV) bounded by the lower and higher volume limits. At these volume extrema, energy increases steeply upon further structural compression or

https://doi.org/10.1021/acs.chemmater.1c03236
Chem. Mater. XXXX, XXX, XXX−XXX

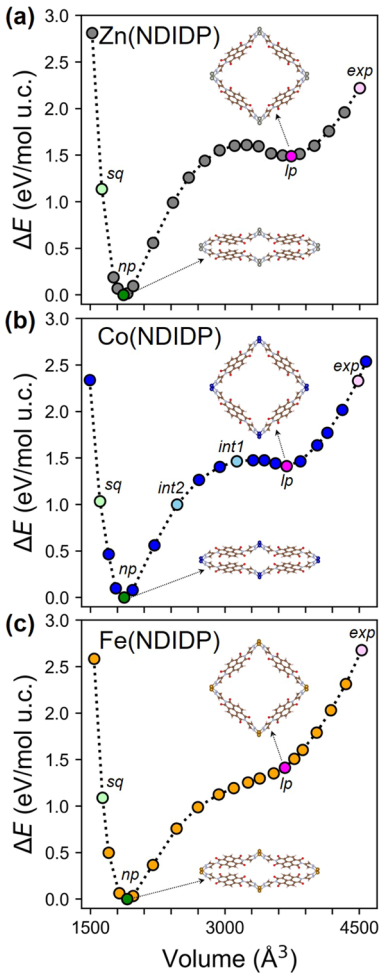

Figure 2. $E(V)$ profiles of (a) Zn(NDIDP), (b) Co(NDIDP), and (c) Fe(NDIDP). Dark green and magenta points correspond to the (meta)stable *np* phase and *lp* phase of the MOFs, for which the corresponding MOF configurations are shown as insets. Lighter green and lighter magenta points indicate the squeezed (*sq*) and expanded (*exp*) configurations discussed later. Light blue points for Co(NDIDP) indicate intermediate (*int*1 and *int*2) configurations that are also discussed later. Further structural information of the highlighted phases is shared in Table S1.

expansion that surpasses the range of motion allowed by the flexible MOFs. Provided that a multitude of energetically accessible configurations are observed over a wide volume range as opposed to the case of rigid MOFs,[69−71] one can conclude that M(NDIDP) MOFs have the potential to show framework flexibility.

The global energy minima of the three M(NDIDP) MOFs are found in the lower volume regime, at V = 1867.6, 1875.2, and 1908.3 Å^3 for Zn, Co, and Fe(NDIDP), respectively. MOF configurations at these volumes (see Figure 2 insets and Figures S1−S3) correspond to the narrow pore (*np*) phase, and hence, all three M(NDIDP) MOFs are expected to energetically favor existing the *np* phase over other structural configurations at 0 K. Interestingly, another energy minimum is found at V = 3735.4 Å^3 for Zn(NDIDP) and also for Co(NDIDP) at V = 3688.9 Å^3, which correspond to a metastable large pore (*lp*) phase. In the case of Fe(NDIDP), however, such an additional *lp* energy minimum is not observed, and the *np* phase is the only thermodynamically stable structural configuration. Nonetheless, the $E(V)$ profile of Fe(NDIDP) is far from being strictly parabolic and displays a large, shoulder-like feature in the higher volume range. This indicates that the higher volume configurations of Fe(NDIDP) are still energetically accessible, yet these configurations cannot be stably sustained by the framework at 0 K. Such a difference in the $E(V)$ profiles can be attributed to the unique binding tendency of Fe, which is more lenient toward configurational changes around the coordination environment. This effect is reflected by the changes in the bond order between the metal ion and the pyrazolate N atom (see Table S2). As such, one can deduce that the binding tendency of the metal ion determines the stability of the additional, metastable *lp* phase that could be exhibited by the MOF. For the sake of consistency in the analyses that follow, the V = 3667.4 Å^3 configuration of Fe(NDIDP) was chosen to serve as the *lp* phase, as it is the closest in the unit cell volume to Zn(NDIDP)−*lp* and Co(NDIDP)−*lp*.

Having installed the redox-active NDI moieties to induce CT, their relative arrangements within M(NDIDP) under the different, energetically accessible configurations were studied. Figure 3 shows the internal NDI arrangements of Co(NDIDP) in the (meta)stable *lp* and *np* phases as a case study. In Co(NDIDP)−*lp*, NDI moieties are arranged in a parallel-displaced manner along the *z*-axis. The stacking distance

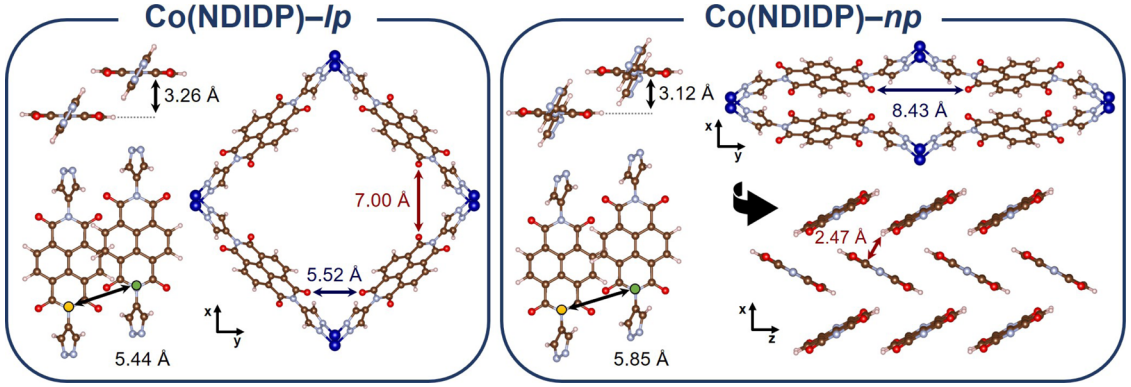

Figure 3. Internal arrangement of the NDI moieties in Co(NDIDP)−*lp* and Co(NDIDP)−*np*. The parallel stacking distance (top left of each panel) and the planar alignment offset (bottom left of each panel) in the *z*-direction, as well as the inter-NDI distances in the *x*- and *y*-directions (right of each panel), are presented. As for the *np* phase, herringbone packing configuration of NDI moieties is separately shown with their edge-to-face distance.

https://doi.org/10.1021/acs.chemmater.1c03236
Chem. Mater. XXXX, XXX, XXX−XXX

between adjacent NDI moieties is 3.26 Å, and the planar alignment offset is 5.44 Å. These distances constitute reasonable contact between NDI moieties for the π orbital overlap, which is essential for the anticipated CT. Along the *x*-axis (resp. *y*-axis), the inter-NDI distance surpasses 7.00 Å (resp. 5.52 Å) at the closest contact (i.e., N−O distance between imides of adjacent NDI), effectively prohibiting the π orbital overlap in these directions. In Co(NDIDP)−*np*, NDI moieties retain their parallel-displaced configuration along the *z*-axis, but with notable differences from the *lp* phase. The stacking distance between NDI moieties is decreased to 3.12 Å, and the planar alignment is increased to 5.85 Å. Interestingly, the contraction of the framework into the *np* phase also leads to edge-to-face interactions between adjacent NDIs along the *x*-axis, as evidenced by the short NDI−H distances of 2.47 Å. Such a tightly packed configuration with the onset of additional, edge-to-face interactions is expected to restrict the conformational freedom of NDI, which could further promote efficient CT. The inter-NDI distances along the *y*-axis surpass 8.43 Å, further prohibiting orbital overlap in this direction. Hence, Co(NDIDP)−*np* exhibits 2D, herringbone packing of NDI in the *xz*-plane, where the orbital overlap between NDI moieties could extend along the two packing dimensions. As shown in Table S3, similar internal NDI arrangements in the *lp* and *np* phases are also found in Zn(NDIDP) and Fe(NDIDP). All in all, vastly distinct internal NDI arrangements are observed in the different structural configurations of M-(NDIDP), which could give rise to notably different CT properties.

Flexibility of M(NDIDP): Pressure vs Volume Equation of State. For a MOF to be truly flexible, transitions between different metastable phases and structural configurations must be possible. Hence, the thermodynamic feasibility of structural transitions in M(NDIDP) MOFs was subsequently investigated. By doing so, we specifically focused on the pressure-induced structural transitions in M(NDIDP) materials, where external pressure or mechanical stress is used as the stimulus. To this end, DFT-based force fields were derived using the QuickFF software for each of the three M(NDIDP) MOFs, and their pressure-versus-volume or $P(V)$ equations of state at T = 300 K were derived following the established protocol,[56,72] resulting in the profiles shown in Figure 4.

Owing to their structural motif, the three M(NDIDP) structures exhibit $P(V)$ equations of state similar to other wine rack MOFs.[27,56,73] In particular, an intermediate, mechanically unstable region with positive $\partial P/\partial V$ values is found to separate two mechanically stable *np* and *lp* branches, which extend toward low volumes (below 2250 Å^3) and high volumes [above 3340 Å^3 for Fe(NDIDP), 3740 Å^3 for Co(NDIDP), and 3790 Å^3 for Zn(NDIDP)]. Each point on these two mechanically stable branches can, in principle, be thermodynamically stabilized by applying suitable isotropic stress, either positive or negative in sign, given by the pressure value at the specific volume point. Provided the presence of two separate, mechanically stable branches in the $P(V)$ equation of state, one can conclude that framework flexibility has been successfully manifested in M(NDIDP) MOFs at room temperature. At atmospheric pressure, that is, P = 0.1 MPa, two (meta)stable intersections with negative $\partial P/\partial V$ values are found for Zn(NDIDP) and Co(NDIDP), whereas only one is found in the lower volume range for Fe(NDIDP). These results are in accordance with the DFT-derived $E(V)$ profiles, as they confirm the thermodynamic (meta)stability of both *lp* and *np*

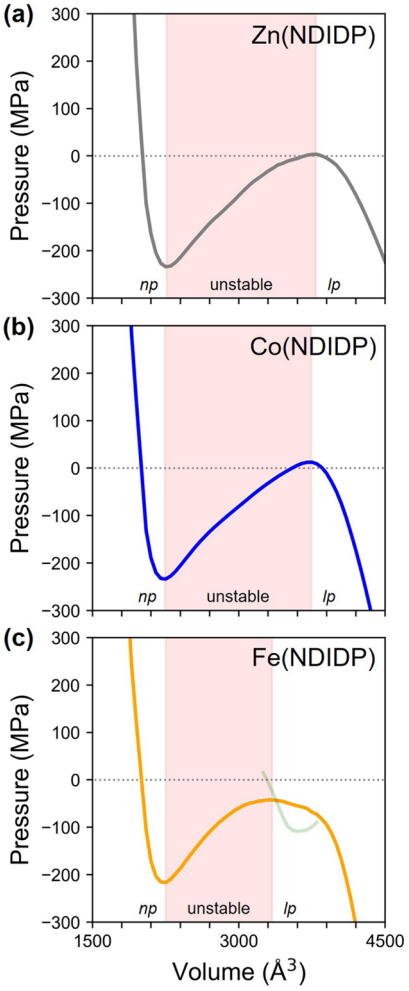

Figure 4. $P(V)$ equations of state at T = 300 K for (a) Zn(NDIDP), (b) Co(NDIDP), and (c) Fe(NDIDP). A gray dotted line pertaining to the ambient pressure is drawn at 0.1 MPa. Regions shaded in red indicate the mechanically unstable volume range, as determined by positive $\partial P/\partial V$ values. In the case of Fe(NDIDP), a secondary partial $P(V)$ curve is shown in light green. This corresponds to the sheared configurations that have deviated away from the main mode of flexibility along the *x*-axis, as discussed in more detail in the Supporting Information.

phases under ambient conditions for Zn(NDIDP) and Co(NDIDP). Correspondingly, in Fe(NDIDP), the $P(V)$ equation of state shows thermodynamic stability only for the *np* phase at atmospheric pressure.

Next, the critical pressures needed to induce structural transitions between the *lp* and *np* phases were extracted. From the $P(V)$ equation of state, they can be determined by identifying the local minimum and maximum in the pressure profile. In Zn(NDIDP), the equation of state shows a pressure minimum at −234 MPa and a maximum at 3 MPa, which can be identified with the *np*-to-*lp* and *lp*-to-*np* transition pressures, respectively. As for Co(NDIDP), these transition pressures are −224 and 13 MPa. For the softer Fe(NDIDP) MOF, these pressures amount to −217 and −42 MPa. Hence, while the *lp*-to-*np* transition in either Zn(NDIDP) or Co(NDIDP) can be easily induced by applying an external pressure of 3 and 13 MPa, the same transition in Fe(NDIDP), as well as the *np*-to-*lp* transitions in all three materials, would require negative pressures. Note that such negative pressures are not yet

https://doi.org/10.1021/acs.chemmater.1c03236
Chem. Mater. XXXX, XXX, XXX−XXX

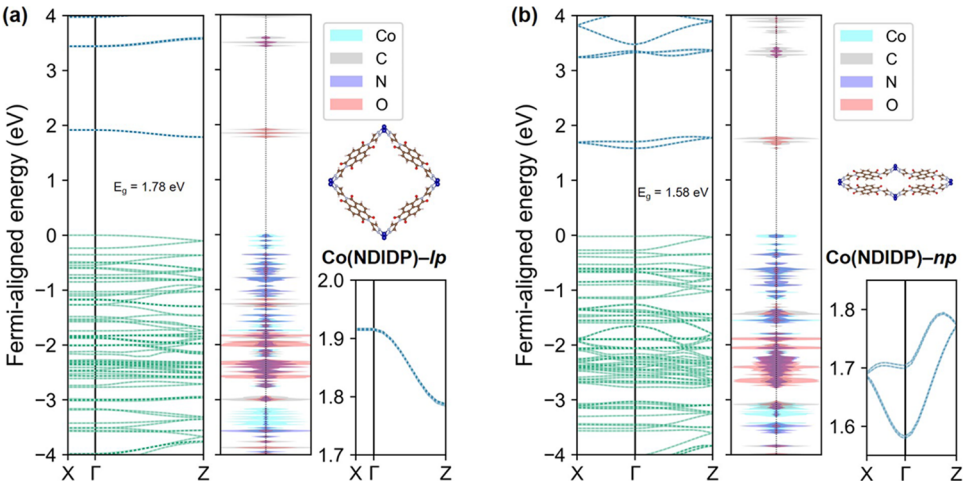

Figure 5. Electronic band structures and projected density of states (PDOS) of (a) Co(NDIDP)−*lp* and (b) Co(NDIDP)−*np*. Conduction band minima corresponding to NDI are shown separately in the bottom right. Green bands are filled valence bands, and blue bands are empty conduction bands. Solid and dotted bands (with lighter color) correspond to up and down spins.

practically achieved in MOFs. Nonetheless, one can envision that finite pulling forces of the corresponding magnitude (applied via embedding the MOF into a flexible membrane, etc.) would induce the *np*-to-*lp* transition.

An interesting feature found in the $P(V)$ equations of state is an anomaly in the curve around V = ∼1650 Å^3, at elevated pressures of ca. 1.5 GPa (Figure S4). Structural configurations to the right of the anomaly (higher volume, Figure S5) closely resemble the *np* phase and retain the four-fold rotational symmetry around the 1D metal clusters. On the other hand, configurations to the left of the anomaly (lower volume, Figure S6) are all rotationally distorted around the metal clusters, and the four-fold symmetry is reduced to two-fold symmetry. This means that at higher pressures, the framework becomes rotationally distorted to alleviate the stress being exerted. Note that the reduction of the rotational symmetry interestingly improves the parallel alignment between adjacent NDI moieties, which could be more favorable for the π orbital overlap and CT. As such, it can be conjectured that by applying pressures of ∼1.5 GPa or higher, rotational distortions could be induced in M(NDIDP), which could potentially lead to further enhancements in their electrical conductivity. Here, we additionally note that in the case of Fe(NDIDP), a separate $P(V)$ curve was observed for the volume range between 3250 and 3800 Å^3 (see the Supporting Information). Corresponding structural configurations are shown in Figure S7, and they are all found to be sheared in the *z*-axial direction compared to the main configurations. As these configurations deviate away from the main mode of flexibility under interest here (i.e., expansion/contraction based on the wine rack motif), we did not further investigate them. Nonetheless, this hints that other modes of flexibility could also exist in M(NDIDP), giving rise to more structural configurations with their own, unique NDI arrangements and resulting CT properties.

Electrical Conductivity of M(NDIDP) and Configuration-Dependent CT. Following the thorough affirmation of their framework flexibility, M(NDIDP) MOFs were analyzed to determine whether or not electrical conductivity has been successfully induced. In order for a MOF to harness conductivity, it must be engineered with long-range CT pathways for electron or hole transport.[11,12] As for M(NDIDP), the installation of redox-active NDI as the central linker moieties and their closely packed arrangement within the framework are expected to provide the CT pathways necessary for conductivity. Computationally, the presence of valid CT pathways in a MOF can be deduced from its electronic band structure via DFT calculations. Note that the effective mass of the charge carriers can be described as follows:

$$\frac{1}{m^*} = \frac{1}{\hbar^2}\frac{\partial^2 E}{\partial k^2}$$

Here, one can see that highly dispersive frontier bands would lead to large curvatures and $\partial^2 E/\partial k^2$ values, giving rise to small effective carrier mass for high carrier mobility during CT, which hence confirms the presence of effective CT pathways for electrical conductivity. As such, electronic band structures of each of the M(NDIDP) MOFs were calculated using DFT methods, and the resulting dispersions of the frontier bands were extensively analyzed to determine whether our modular design approach has successfully secured the valid CT pathways with low effective carrier mass in these materials.

Electronic band structures and projected density of states (PDOS) of Co(NDIDP) are presented in Figure 5, and those of Zn(NDIDP) and Fe(NDIDP) are shown in Figures S8 and S9, respectively. Band structures are drawn along the Γ−*X* and Γ−*Z* high symmetry paths, which directly correspond to the *x*- and *z*-axial directions, along which close-packing of the NDI units was previously observed. Given their dissimilar NDI arrangements, calculations were performed for both *lp* and *np* phases. Remarkably, the band structures of all three M(NDIDP)s in both phases exhibit notable dispersion in their conduction band minimum (CBM), which is ideal for CT. From the PDOS and band-decomposed charge density plots (Figure S10), sole contributors to the CBM are revealed to be the C and O atoms of the NDI moieties. This shows that the CBMs of M(NDIDP) MOFs are exclusively composed of the orbitals provided by NDI. The dispersion of the CBM hence arises from the orbital overlap between closely packed NDI units, which effectively completes the CT pathways in M(NDIDP) MOFs as intended by our modular design approach. Band gaps (E_g) of the MOFs under the two phases are found well within the semiconducting range,[12] with values

https://doi.org/10.1021/acs.chemmater.1c03236
Chem. Mater. XXXX, XXX, XXX−XXX

Table 1. CBM Dispersion Values and Corresponding Effective Masses of Electrons (m_e*) Obtained from the Band Structures of M(NDIDP)−*lp* and M(NDIDP)−*np* (m_0: Electron Rest Mass)

	large pore (*lp*)		narrow pore (*np*)	
M(NDIDP)	Γ−*X*	Γ−*Z*	Γ−*X*	Γ−*Z*
Zn	∼0 meVm_e* → ∞	83 meV	73 meV	200 meV
		m_e* = 4.37m_0	m_e* = 3.02m_0	m_e* = 1.51m_0
Co		130 meV	121 meV	211 meV
		m_e* = 2.76m_0	m_e* = 2.36 m_0	m_e* = 1.64m_0
Fe		212 meV	403 meV	633 meV
		m_e* = 1.71m_0	m_e* = 1.17m_0	m_e* = 0.73m_0

ranging between 0.16 and 2.39 eV (see Figures 5, S8, and S9). As such, all three MOFs in both *lp* and *np* phases harness the potential to exhibit electrical conductivity, which can be triggered by populating the CBM with electrons via excitation or n-doping of the system. Note that large dispersions are also present in the valence band maximum (VBM) in some cases, especially for Fe(NDIDP). Such VBM dispersions are suspected to be artifacts of the DFT methods adopted in our study and should not be directly interpreted as certain indications of efficient hole transport (see the Supporting Information).

In M(NDIDP)−*lp*, the dispersion of the CBM is limited to the Γ−*Z* path, and the band remains strictly flat along the Γ−*X* path. This is in accordance with the internal NDI arrangement observed in the *lp* phase, where parallel-displaced packing along the *z*-axis was found. As such, CT in M(NDIDP)−*lp* is expected to propagate one-dimensionally along the *z*-axis. Dispersion is measured to be 83, 130, and 212 meV for Zn, Co, and Fe(NDIDP)−*lp*, respectively. Here, we note the increasing trend of CBM dispersion in the presented order of MOFs. This is also attributed to the different binding tendencies of metal ions, which become softer from Zn to Co, then Fe. Softer metal ions would allow the MOF to further distort its structure, better optimizing the orbital overlap between stacked NDI moieties. This is indeed corroborated by their internal NDI arrangements (see Table S3), where the adjacent NDI moieties become more parallelly aligned in the same order. Electron effective mass at the CBM edges (m_e*) was also calculated and is presented in Table 1. Although m_e* values along the Γ−*Z* path in M(NDIDP)−*lp* are relatively high, they still constitute significant improvements over the nonconducting case (i.e., m_e* → ∞), hence effectively validating the presence of CT pathways.

Upon discussing the case of M(NDIDP)−*np*, we first note the breaking of energy degeneracy in the CBM at the Γ point. Such a phenomenon arises from the presence of two pairs of NDI moieties within the chosen M(NDIDP) unit cell, which newly comes in contact with one another along the *x*-axis in the *np* phase (see Figure 3). Consequently, interactions among the NDI pairs cause the CBM to break the originally observed energy degeneracy between four NDI moieties at the Γ point. Note that a single NDI moiety serves as one electronic unit, yet the unit cell of M(NDIDP)−*np* contains two electronic units along both *x* and *z*-axes (see the Supporting Information). Therefore, the CBM should be understood as having been folded because of the presence of multiple electronic units within the unit cell.[74] This interpretation is further substantiated by the convergence of CBM and CBM + 1 band energies observed at the *X* and *Z* symmetry points. As such, a set of bands all corresponding to the lowest unoccupied orbitals of NDI was collectively regarded as the CBM, and band dispersion and m_e* were calculated accordingly.

The CBM of M(NDIDP)−*np* along the Γ−*Z* path shows significant dispersions of 200, 211, and 633 meV for Zn, Co, and Fe(NDIDP)−*np*, respectively, all of which have increased compared to the *lp* phase. This can be attributed to the tighter packing of NDI along the *z*-axis (see Table S3), which improves the orbital overlap between adjacent NDI moieties. More importantly, band dispersion is newly observed along the Γ−*X* path as well in all three MOFs. This confirms that 2D herringbone packing of NDI exhibited by M(NDIDP)−*np* can provide sufficient orbital overlap along both dimensions, resulting in 2D CT. Dispersions along the Γ−*X* path are 73, 121, and 403 meV for Zn, Co, and Fe(NDIDP)−*np*, respectively, which are comparable to the Γ−*Z* path in M(NDIDP)−*lp*. Trends in the band dispersion are correspondingly carried over to m_e* (see Table 1), where m_e* is reduced along the Γ−*Z* path compared to M(NDIDP)−*lp*, and finite m_e* values are newly observed along the Γ−*X* path. Note that E_g of Co(NDIDP) decreases from 1.78 to 1.58 eV as the MOF transitions from the *lp* to *np* phase. A similar reduction of E_g is observed for the other two MOFs (see Figures S8 and S9), where E_g decreases from 2.39 to 2.20 eV and from 0.54 to 0.16 eV in Zn and Fe(NDIDP), respectively. These changes in E_g are consistent with what was previously reported for MIL-47 and MIL-53.[31]

Note that results thus far were obtained for the MOF configurations optimized at the DFT-D3(BJ) level of theory. To investigate the sensitivity of trends in CT properties to the consideration of the self-interaction error during geometry optimization, additional calculations were performed at the DFT + U-D3(BJ) level of theory. Results, shared in the Supporting Information, show that the transition from 1D to 2D charge transport from the *lp* phase to the *np* phase is consistently observed. Altogether, significant conductivity can be predicted for all three M(NDIDP)s based on their dispersive frontier bands, and their precise CT properties are found to vary drastically, depending on the structural configurations. Between the *lp* and *np* phases, differences in the CT properties are characterized by increased band dispersion and transition from 1D to 2D transport. Such differences are explained by changes in the internal NDI arrangement, which progresses from 1D parallel-displaced packing to 2D herringbone packing as the MOF transitions from the *lp* to the *np* phase.

Further Exploration of Configuration-Dependent CT. Based on the findings thus far, we conclude that two material properties, namely, flexibility and conductivity, have been successfully instilled and synergistically combined in M(NDIDP), resulting in their tunable electrical conductivity arising from configuration-dependent CT properties. Next, one

https://doi.org/10.1021/acs.chemmater.1c03236
Chem. Mater. XXXX, XXX, XXX−XXX

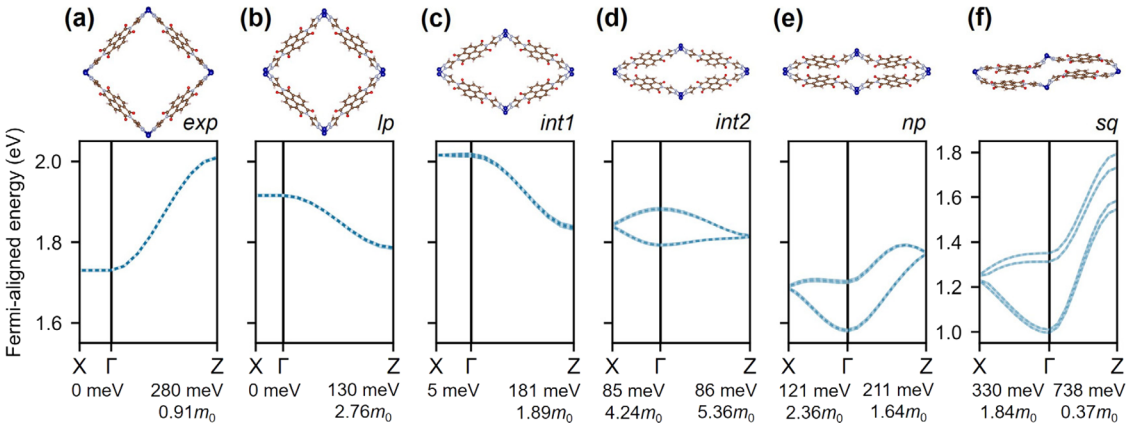

Figure 6. Evolution of the CBM of Co(NDIDP) upon decreasing volume under all of the structural configurations considered. Full electronic band structures of the additional structural configurations (*exp*, *int*1, *int*2, and *sq*) are shared in Figure S13. Solid (blue) and dotted bands (lighter blue) correspond to up and down spins.

could envisage that CT properties of M(NDIDP) could be further tuned by taking advantage of their flexibility and exploring more of their allowed structural configurations. Hence, additional structural configurations of M(NDIDP) were selected and analyzed for their unique CT properties. Two intermediate configurations located between the *lp* and *np* phases, herein referred to as *int*1 and *int*2, were first extracted (light blue points in Figure 2). Additionally, "squeezed" (*sq*) and "expanded" (*exp*) configurations were obtained as structures smaller than the *np* phase or larger than the *lp* phase, respectively, whilst exhibiting an energy difference of less than 1.5 eV from the corresponding phases at 0 K (light green and light magenta points in Figure 2). While these configurations are not thermodynamically accessible under ambient conditions, they are still of considerable interest because external stimuli (e.g., guest loading, mechanical stress, and isotropic pulling) could effectively lead to their stabilization. Band structures were subsequently calculated for the chosen configurations in Co(NDIDP) (Figures S11 and S12), and the results are presented in Figures 6 and S13.

In Co(NDIDP)−*exp* (Figure 6a), where the MOF is further expanded past the *lp* phase (Figure 6b), significant enhancement in CT is interestingly observed. While the CBM remains flat along the Γ−*X* path, band dispersion along the Γ−*Z* path increases from 130 to 280 meV, and m_e* decreases from 2.76m_0 to 0.91m_0. E_g is found to be 1.73 eV (see Figure S13), which is slightly lower than that of Co(NDIDP)−*lp*. It is also noted that the energy of the CBM at the *Z* point is higher than the energy at the Γ point, whereas the inverse trend was observed in the *lp* phase. These phenomena are collectively attributed to the reconfiguration of NDI moieties accompanying further framework expansion (see Table S3). The internal NDI arrangement of Co(NDIDP)−*exp* exhibits a notable decrease in the *z*-axial stacking distance from 3.26 (*lp*) to 3.12 Å (*exp*), which improves the orbital overlap between NDI moieties and therefore explains the increased band dispersion. Concurrently, the planar alignment offset surges from 5.44 (*lp*) to 6.63 Å (*exp*). Such a large difference in the NDI alignment is significant enough to induce a change of sign in the transfer integral between adjacent moieties, hence inverting the energy trend along the Γ−*Z* path. As presented in Figure S14, notably enhanced CT properties are consistently observed in Zn(NDIDP)−*exp* and Fe(NDIDP)−*exp* as well (structures shown in Figure S15) compared to their *lp* counterparts. This effectively demonstrates that if M(NDIDP) can be further expanded past the *lp* phase, for instance, by an isotropic pulling of the material, their CT properties and the resulting conductivity would be notably enhanced.

Next, two intermediate *int*1 and *int*2 configurations (Figure 6c) between the metastable *lp* and *np* phases were analyzed, which allow one to study the evolution of the CBM as Co(NDIDP) undergoes the *lp*-to-*np* transition. Along the Γ−*X* path, dispersion is found to monotonically increase as follows: 0 meV (*lp*), 5 meV (*int*1), 85 meV (*int*2), and 121 meV (*np*). This trend is straightforwardly explained by the effect of framework contraction on the internal NDI arrangement of Co(NDIDP) (see Tables S2). Pairs of NDI moieties along the *x*-axis become closer to each other from one configuration to the next, leading to the gradual onset of their orbital overlap and CT in the *x*-axial direction. Along the Γ−*Z* path, band dispersions are 130 meV (*lp*), 181 meV (*int*1), 86 meV (*int*2), and 211 meV (*np*). Curiously, band dispersion decreases in Co(NDIDP)−*int*2, while the other three configurations show an increasing trend. This can be attributed to the large *z*-axial stacking distance of 3.6 Å observed in Co(NDIDP)−*int*2 as opposed to 3.26 Å (*lp*), 3.40 Å (*int*1), and 3.12 Å (*np*), which has significantly increased to better accommodate the pair interactions newly taking place in the *x*-axial direction. These results demonstrate that the correlation between the structural transition of M(NDIDP) and the resulting CT properties is nonlinear and rather complex. Nonetheless, a gradual transition from 1D to 2D transport is undoubtedly observed, establishing that the CT properties and the resulting conductivity of M(NDIDP) MOFs can be finely tuned by accessing the intermediate configurations between the *lp* and *np* phases.

Remarkably, the contraction of Co(NDIDP) past the *np* phase (Figure 6e) to Co(NDIDP)−*sq* (Figure 6f) also results in large dispersions in the CBM. In Co(NDIDP)−*sq*, CBM dispersion is measured to be 330 and 738 meV along the Γ−*X* and Γ−*Z* paths. These values constitute substantial enhancement over the case of Co(NDIDP)−*np*, especially along the Γ−*Z* path, where the dispersion has increased by a factor of 3.5. Large dispersion in the CBM leads to significantly smaller m_e*, where the effective mass is reduced from 2.36m_0 to 1.84m_0 along the Γ−*X* path, and from 1.64m_0 to 0.37m_0 along the Γ−*Z* path. Carrier effective mass of 0.37m_0 is one of the lowest values that has been calculated for a MOF, to the best of

https://doi.org/10.1021/acs.chemmater.1c03236
Chem. Mater. XXXX, XXX, XXX−XXX

our knowledge.[75,76] E_g is significantly decreased from 1.58 eV (*np*) to 1.00 eV (*sq*) (see Figure S13). Again, such marked improvements are associated with the internal NDI arrangement of Co(NDIDP)−*sq* (see Table S3). In this structural configuration, NDI moieties are even more tightly packed together: the *z*-axial stacking distance is reduced from 3.12 to 2.14 Å, and the NDI−H distance is also reduced from 2.47 to 2.16 Å. This effectively maximizes the orbital overlap between adjacent NDI moieties, which can further boost CT and the resulting conductivity. Note that the extreme contraction of Co(NDIDP) into the *sq* configuration leads to an uneven spacing between NDI moieties in the *z*-axial direction (see Figure S16), which creates an opening between the folded bands of the CBM at the *Z* point. Based on these results, we conclude that significantly enhanced CT properties of Co(NDIDP) could be attained by further contracting or compressing the MOF past the *np* phase, which could then lead to notably improved conductivity.

Similar CT enhancements were not observed in the readily procured *sq* configurations of Zn(NDIDP) and Fe(NDIDP) (Figures S17 and S18). In the case of Zn(NDIDP)−*sq*, only a 1.33-fold increase in the band dispersion is observed compared to the *np* phase. As for Fe(NDIDP)−*sq*, band dispersion has rather diminished compared to Fe(NDIDP)−*np* along both symmetry paths. We attribute these differences in CT properties to the visibly different structural configuration of Co(NDIDP)−*sq* (see Figure S12) as opposed to Zn or Fe(NDIDP)−*sq* (see Figure S17), where a counter-clockwise rotational distortion around the 1D metal cluster is observed. Such rotational distortion around the 1D metal cluster has also been computationally predicted for the low volume configurations of other wine rack MOFs in previous studies.[77−80] As conjectured previously, this distortion induces a much smaller angle between the edge-to-face NDI pairs compared to Co(NDIDP)−*np*, Zn(NDIDP)−*sq*, or Fe(NDIDP)−*sq* (see Table S3), which is highly beneficial for the π-orbital overlap. As a result, notable CT enhancement of Co(NDIDP)−*sq* is attributed to the observed rotational distortion. Note that similarly distorted structural configurations of Zn(NDIDP) and Fe(NDIDP) were nonetheless observed from the MD simulations (see Figure S6) for lower unit cell volumes (<1650 Å^3) at room temperature. Hence, it is predicted that framework contraction past the *np* phase could lead to the greatest improvements in CT properties for all three M(NDIDP) MOFs, as long as the rotational distortion around the metal cluster simultaneously takes place. Altogether, our analysis effectively demonstrates that configuration-dependent CT properties of M(NDIDP) lead to their tunable electrical conductivity, and many other structural configurations with unique CT properties exist for these flexible MOFs.

CONCLUSIONS

In this study, we have demonstrated that framework flexibility and electrical conductivity can be synergistically combined into a single MOF via a modular design approach. The designed MOFs, M(NDIDP) with M = Zn, Co, and Fe, show significant framework flexibility and are capable of pressure-induced structural transitions at low pressures and room temperature. M(NDIDP) MOFs also exhibit configuration-dependent CT properties, which are characterized by transition from 1D to 2D transport and up to 5.7-fold increase in band dispersion (7.5-fold reduction in effective carrier mass) between different structural configurations. As a result, tunable electrical conductivity is predicted for the M(NDIDP) MOFs, where the degree of CT in the MOF can be controlled via the application of external stimuli (e.g., mechanical stress, temperature, light, and guest adsorption). The design of flexible and electrically conductive MOFs performed in this work demonstrates the practicability of simultaneously inducing multiple material properties in the same MOF via the modular design approach. We anticipate that our design approach can be extended to discover more flexible and conductive MOFs for adsorptive sensing, conformal electronics, molecular switches, and many other relevant applications that may benefit from stimuli-induced changes in electrical conductivity.

ASSOCIATED CONTENT

Supporting Information

The Supporting Information is available free of charge at https://pubs.acs.org/doi/10.1021/acs.chemmater.1c03236.

Structures of M(NDIDP) in *lp* and *np* phases; *P*(*V*) equation of state in the low *V* range and corresponding configurations; secondary-phase structures of Fe(NDIDP); band structures of Zn(NDIDP) and Fe(NDIDP) in *lp* and *np* phases; band-decomposed charge density plots of the CBM of M(NDIDP); additional structural configurations of Co(NDIDP) and their band structures; structures and band structures of the *exp* configuration of Zn and Fe(NDIDP); NDI arrangement in the z-axial direction for Co(NDIDP)−*sq*; structures and band structures of the *sq* configuration of Zn and Fe(NDIDP); atom-type assignment in M(NDIDP) for force-field generation; lattice parameters of M(NDIDP); internal NDI arrangements of M(NDIDP); flexibility and conductivity of Zn(NDIDP)-CH_3; secondary-phase configurations of Fe(NDIDP); VBM dispersion in M(NDIDP); CBM splitting/folding in smaller volume configurations; calculations at the DFT+U theory-level; Brillouin zone plots for M(NDIDP)−*lp* and M(NDIDP)−*np*; and data availability (PDF)

AUTHOR INFORMATION

Corresponding Author

Jihan Kim − *Department of Chemical and Biomolecular Engineering, Korea Advanced Institute of Science and Technology (KAIST), Daejeon 34141, South Korea;* orcid.org/0000-0002-3844-8789; Email: jihankim@kaist.ac.kr

Authors

Sanggyu Chong − *Department of Chemical and Biomolecular Engineering, Korea Advanced Institute of Science and Technology (KAIST), Daejeon 34141, South Korea;* orcid.org/0000-0002-6948-1602

Sven M. J. Rogge − *Center for Molecular Modeling (CMM), Ghent University, Zwijnaarde 9052, Belgium;* orcid.org/0000-0003-4493-5708

Complete contact information is available at: https://pubs.acs.org/10.1021/acs.chemmater.1c03236

Author Contributions

[§]S.C. and S.M.J.R. contributed equally to this work

Notes

The authors declare no competing financial interest.

https://doi.org/10.1021/acs.chemmater.1c03236
Chem. Mater. XXXX, XXX, XXX−XXX

■ ACKNOWLEDGMENTS

S.C. thanks the National Research Foundation (NRF) and Ministry of Education (MOE) of Korea for the Global Ph.D. Fellowship (no. 2019H1A2A1075192). S.M.J.R. acknowledges support from the Fund for Scientific Research − Flanders (FWO) through a junior postdoctoral fellowship (grant no. 12T3519N). S.C. and J.K. acknowledge support from the NRF of Korea grant funded by the Korean government (MSIT) (no. 2021R1A2C2003583). This research utilized the computing resources of KISTI National Supercomputing Center (KSC-2020-CRE-0052) as well as the Stevin Supercomputer Infrastructure, the latter provided by the VSC (Flemish Supercomputer Centre), funded by Ghent University, the Research Foundation − Flanders (FWO), and the Flemish Government − department EWI. The authors acknowledge Sander Borgmans for insightful discussions.

■ REFERENCES

(1) Guillerm, V.; Kim, D.; Eubank, J. F.; Luebke, R.; Liu, X.; Adil, K.; Lah, M. S.; Eddaoudi, M. A Supermolecular Building Approach for the Design and Construction of Metal−Organic Frameworks. *Chem. Soc. Rev.* **2014**, *43*, 6141−6172.

(2) Yao, Z.; Sánchez-Lengeling, B.; Bobbitt, N. S.; Bucior, B. J.; Kumar, S. G. H.; Collins, S. P.; Burns, T.; Woo, T. K.; Farha, O. K.; Snurr, R. Q.; Aspuru-Guzik, A. Inverse Design of Nanoporous Crystalline Reticular Materials with Deep Generative Models. *Nat. Mach. Intell.* **2021**, *3*, 76−86.

(3) Lee, S.; Kim, B.; Cho, H.; Lee, H.; Lee, S. Y.; Cho, E. S.; Kim, J. Computational Screening of Trillions of Metal−Organic Frameworks for High-Performance Methane Storage. *ACS Appl. Mater. Interfaces* **2021**, *13*, 23647−23654.

(4) Fang, Z.; Bueken, B.; de Vos, D. E.; Fischer, R. A. Defect-Engineered Metal−Organic Frameworks. *Angew. Chem., Int. Ed.* **2015**, *54*, 7234−7254.

(5) Chong, S.; Thiele, G.; Kim, J. Excavating Hidden Adsorption Sites in Metal−Organic Frameworks Using Rational Defect Engineering. *Nat. Commun.* **2017**, *8*, 1539.

(6) Boyd, P. G.; Chidambaram, A.; García-Díez, E.; Ireland, C. P.; Daff, T. D.; Bounds, R.; Gładysiak, A.; Schouwink, P.; Moosavi, S. M.; Maroto-Valer, M. M.; Reimer, J. A.; Navarro, J. A. R.; Woo, T. K.; Garcia, S.; Stylianou, K. C.; Smit, B. Data-Driven Design of Metal−Organic Frameworks for Wet Flue Gas CO_2 Capture. *Nature* **2019**, *576*, 253−256.

(7) Rosen, A. S.; Notestein, J. M.; Snurr, R. Q. Structure-Activity Relationships That Identify Metal−Organic Framework Catalysts for Methane Activation. *ACS Catal.* **2019**, *9*, 3576−3587.

(8) Teplensky, M. H.; Fantham, M.; Li, P.; Wang, T. C.; Mehta, J. P.; Young, L. J.; Moghadam, P. Z.; Hupp, J. T.; Farha, O. K.; Kaminski, C. F.; Fairen-Jimenez, D. Temperature Treatment of Highly Porous Zirconium-Containing Metal−Organic Frameworks Extends Drug Delivery Release. *J. Am. Chem. Soc.* **2017**, *139*, 7522−7532.

(9) Kim, H.; Yang, S.; Rao, S. R.; Narayanan, S.; Kapustin, E. A.; Furukawa, H.; Umans, A. S.; Yaghi, O. M.; Wang, E. N. Water Harvesting from Air with Metal−Organic Frameworks Powered by Natural Sunlight. *Science* **2017**, *356*, 430−434.

(10) Suh, B. L.; Chong, S.; Kim, J. Photochemically Induced Water Harvesting in Metal−Organic Framework. *ACS Sustainable Chem. Eng.* **2019**, *7*, 15854−15859.

(11) Sun, L.; Campbell, M. G.; Dincă, M. Electrically Conductive Porous Metal−Organic Frameworks. *Angew. Chem., Int. Ed.* **2016**, *55*, 3566−3579.

(12) Xie, L. S.; Skorupskii, G.; Dincă, M. Electrically Conductive Metal-Organic Frameworks. *Chem. Rev.* **2020**, *120*, 8536−8580.

(13) Golomb, M. J.; Calbo, J.; Bristow, J. K.; Walsh, A. Ligand Engineering in Cu(ii) Paddle Wheel Metal−Organic Frameworks for Enhanced Semiconductivity. *J. Mater. Chem. A* **2020**, *8*, 13160−13165.

(14) Chong, S.; Kim, J. Rational Modifications of PCN-700 to Induce Electrical Conductivity: A Computational Study. *Dalton Trans.* **2020**, *49*, 102−113.

(15) Chong, S.; Park, D. T.; Kim, J. Exploring Guest-Dependent Photoconductivity in a Donor-Containing Metal−Organic Framework. *J. Phys. Chem. C* **2021**, *125*, 10198−10206.

(16) Huang, X.; Sheng, P.; Tu, Z.; Zhang, F.; Wang, J.; Geng, H.; Zou, Y.; di, C. A.; Yi, Y.; Sun, Y.; Xu, W.; Zhu, D. A Two-Dimensional π−d Conjugated Coordination Polymer with Extremely High Electrical Conductivity and Ambipolar Transport Behaviour. *Nat. Commun.* **2015**, *6*, 7408.

(17) Xie, L. S.; Sun, L.; Wan, R.; Park, S. S.; DeGayner, J. A.; Hendon, C. H.; Dincă, M. Tunable Mixed-Valence Doping toward Record Electrical Conductivity in a Three-Dimensional Metal−Organic Framework. *J. Am. Chem. Soc.* **2018**, *140*, 7411−7414.

(18) Song, X.; Wang, X.; Li, Y.; Zheng, C.; Zhang, B.; di, C. A.; Li, F.; Jin, C.; Mi, W.; Chen, L.; Hu, W. 2D Semiconducting Metal−Organic Framework Thin Films for Organic Spin Valves. *Angew. Chem., Int. Ed.* **2020**, *132*, 1134−1139.

(19) Wu, G.; Huang, J.; Zang, Y.; He, J.; Xu, G. Porous Field-Effect Transistors Based on a Semiconductive Metal−Organic Framework. *J. Am. Chem. Soc.* **2017**, *139*, 1360−1363.

(20) Sheberla, D.; Bachman, J. C.; Elias, J. S.; Sun, C. J.; Shao-Horn, Y.; Dincă, M. Conductive MOF Electrodes for Stable Supercapacitors with High Areal Capacitance. *Nat. Mater.* **2017**, *16*, 220−224.

(21) Campbell, M. G.; Sheberla, D.; Liu, S. F.; Swager, T. M.; Dincă, M. Cu_3(Hexaiminotriphenylene)$_2$: An Electrically Conductive 2D Metal−Organic Framework for Chemiresistive Sensing. *Angew. Chem., Int. Ed.* **2015**, *54*, 4349−4352.

(22) Campbell, M. G.; Liu, S. F.; Swager, T. M.; Dincă, M. Chemiresistive Sensor Arrays from Conductive 2D Metal−Organic Frameworks. *J. Am. Chem. Soc.* **2015**, *137*, 13780−13783.

(23) Meng, Z.; Aykanat, A.; Mirica, K. A. Welding Metallophthalocyanines into Bimetallic Molecular Meshes for Ultrasensitive, Low-Power Chemiresistive Detection of Gases. *J. Am. Chem. Soc.* **2019**, *141*, 2046−2053.

(24) Miner, E. M.; Fukushima, T.; Sheberla, D.; Sun, L.; Surendranath, Y.; Dincă, M. Electrochemical Oxygen Reduction Catalysed by Ni_3(Hexaiminotriphenylene)$_2$. *Nat. Commun.* **2016**, *7*, 10942.

(25) Krause, S.; Hosono, N.; Kitagawa, S. Chemistry of Soft Porous Crystals: Structural Dynamics and Gas Adsorption Properties. *Angew. Chem., Int. Ed.* **2020**, *59*, 15325−15341.

(26) Coudert, F. X. Responsive Metal−Organic Frameworks and Framework Materials: Under Pressure, Taking the Heat, in the Spotlight, with Friends. *Chem. Mater.* **2015**, *27*, 1905−1916.

(27) Vanduyfhuys, L.; Rogge, S. M. J.; Wieme, J.; Vandenbrande, S.; Maurin, G.; Waroquier, M.; Van Speybroeck, V. Thermodynamic Insight into Stimuli-Responsive Behaviour of Soft Porous Crystals. *Nat. Commun.* **2018**, *9*, 204.

(28) Evans, J. D.; Bon, V.; Senkovska, I.; Lee, H.-C.; Kaskel, S. Four-Dimensional Metal−Organic Frameworks. *Nat. Commun.* **2020**, *11*, 2690.

(29) Yanai, N.; Kitayama, K.; Hijikata, Y.; Sato, H.; Matsuda, R.; Kubota, Y.; Takata, M.; Mizuno, M.; Uemura, T.; Kitagawa, S. Gas Detection by Structural Variations of Fluorescent Guest Molecules in a Flexible Porous Coordination Polymer. *Nat. Mater.* **2011**, *10*, 787−793.

(30) Qin, J. S.; Yuan, S.; Alsalme, A.; Zhou, H. C. Flexible Zirconium MOF as the Crystalline Sponge for Coordinative Alignment of Dicarboxylates. *ACS Appl. Mater. Interfaces* **2017**, *9*, 33408−33412.

(31) Ling, S.; Slater, B. Unusually Large Band Gap Changes in Breathing Metal−Organic Framework Materials. *J. Phys. Chem. C* **2015**, *119*, 16667−16677.

https://doi.org/10.1021/acs.chemmater.1c03236
Chem. Mater. XXXX, XXX, XXX−XXX

(32) Choi, H. J.; Dincă, M.; Long, J. R. Broadly Hysteretic H_2 Adsorption in the Microporous Metal−Organic Framework Co(1,4-Benzenedipyrazolate). *J. Am. Chem. Soc.* **2008**, *130*, 7848−7850.
(33) Galli, S.; Masciocchi, N.; Colombo, V.; Maspero, A.; Palmisano, G.; López-Garzón, F. J.; Domingo-García, M.; Fernández-Morales, I.; Barea, E.; Navarro, J. A. R. Adsorption of Harmful Organic Vapors by Flexible Hydrophobic Bis-Pyrazolate Based MOFs. *Chem. Mater.* **2010**, *22*, 1664−1672.
(34) Mason, J. A.; Oktawiec, J.; Taylor, M. K.; Hudson, M. R.; Rodriguez, J.; Bachman, J. E.; Gonzalez, M. I.; Cervellino, A.; Guagliardi, A.; Brown, C. M.; Llewellyn, P. L.; Masciocchi, N.; Long, J. R. Methane Storage in Flexible Metal−Organic Frameworks with Intrinsic Thermal Management. *Nature* **2015**, *527*, 357−361.
(35) Earmme, T.; Hwang, Y. J.; Murari, N. M.; Subramaniyan, S.; Jenekhe, S. A. All-Polymer Solar Cells with 3.3% Efficiency Based on Naphthalene Diimide-Selenophene Copolymer Acceptor. *J. Am. Chem. Soc.* **2013**, *135*, 14960−14963.
(36) Hwang, Y.-J.; Earmme, T.; Courtright, B. A. E.; Eberle, F. N.; Jenekhe, S. A. N-Type Semiconducting Naphthalene Diimide-Perylene Diimide Copolymers: Controlling Crystallinity, Blend Morphology, and Compatibility Toward High-Performance All-Polymer Solar Cells. *J. Am. Chem. Soc.* **2015**, *137*, 4424−4434.
(37) Rundel, K.; Maniam, S.; Deshmukh, K.; Gann, E.; Prasad, S. K. K.; Hodgkiss, J. M.; Langford, S. J.; McNeill, C. R. Naphthalene Diimide-Based Small Molecule Acceptors for Organic Solar Cells. *J. Mater. Chem. A* **2017**, *5*, 12266−12277.
(38) Kresse, G.; Hafner, J. Ab Initio Molecular Dynamics for Liquid Metals. *Phys. Rev. B* **1993**, *47*, 558−561.
(39) Kresse, G.; Furthmüller, J. Efficiency of Ab-Initio Total Energy Calculations for Metals and Semiconductors Using a Plane-Wave Basis Set. *Comput. Mater. Sci.* **1996**, *6*, 15−50.
(40) Kresse, G.; Furthmüller, J. Efficient Iterative Schemes for Ab Initio Total-Energy Calculations Using a Plane-Wave Basis Set. *Phys. Rev. B* **1996**, *54*, 11169−11186.
(41) Blöchl, P. E. Projector Augmented-Wave Method. *Phys. Rev. B* **1994**, *50*, 17953−17979.
(42) Kresse, G.; Joubert, D. From Ultrasoft Pseudopotentials to the Projector Augmented-Wave Method. *Phys. Rev. B* **1999**, *59*, 1758−1775.
(43) Perdew, J. P.; Burke, K.; Ernzerhof, M. Generalized Gradient Approximation Made Simple. *Phys. Rev. Lett.* **1996**, *77*, 3865−3868.
(44) Grimme, S.; Ehrlich, S.; Goerigk, L. Effect of the Damping Function in Dispersion Corrected Density Functional Theory. *J. Comput. Chem.* **2011**, *32*, 1456−1465.
(45) Krukau, A. V.; Vydrov, O. A.; Izmaylov, A. F.; Scuseria, G. E. Influence of the Exchange Screening Parameter on the Performance of Screened Hybrid Functionals. *J. Chem. Phys.* **2006**, *125*, 224106.
(46) Moellmann, J.; Grimme, S. DFT-D3 Study of Some Molecular Crystals. *J. Phys. Chem. C* **2014**, *118*, 7615−7621.
(47) M Ganose, A.; J Jackson, A.; O Scanlon, D. sumo: Command-line tools for plotting and analysis of periodic ab initio calculations. *J. Open Source Softw.* **2018**, *3*, 717.
(48) Vanduyfhuys, L.; Vandenbrande, S.; Verstraelen, T.; Schmid, R.; Waroquier, M.; Van Speybroeck, V. QuickFF: A Program for a Quick and Easy Derivation of Force Fields for Metal-Organic Frameworks from Ab Initio Input. *J. Comput. Chem.* **2015**, *36*, 1015−1027.
(49) Vanduyfhuys, L.; Vandenbrande, S.; Wieme, J.; Waroquier, M.; Verstraelen, T.; Van Speybroeck, V. Extension of the QuickFF Force Field Protocol for an Improved Accuracy of Structural, Vibrational, Mechanical and Thermal Properties of Metal-Organic Frameworks. *J. Comput. Chem.* **2018**, *39*, 999−1011.
(50) Verstraelen, T.; Vandenbrande, S.; Heidar-Zadeh, F.; Vanduyfhuys, L.; Van Speybroeck, V.; Waroquier, M.; Ayers, P. W. Minimal Basis Iterative Stockholder: Atoms in Molecules for Force-Field Development. *J. Chem. Theory Comput.* **2016**, *12*, 3894−3912.
(51) Mortensen, J. J.; Hansen, L. B.; Jacobsen, K. W. Real-Space Grid Implementation of the Projector Augmented Wave Method. *Phys. Rev. B* **2005**, *71*, No. 035109.
(52) Enkovaara, J.; Rostgaard, C.; Mortensen, J. J.; Chen, J.; Dułak, M.; Ferrighi, L.; Gavnholt, J.; Glinsvad, C.; Haikola, V.; Hansen, H. A.; et al. Electronic Structure Calculations with GPAW: A Real-Space Implementation of the Projector Augmented-Wave Method. *J. Phys. Condens. Matter* **2010**, *22*, No. 253202.
(53) Chen, J.; Martínez, T. J. Charge Transfer with Polarization Current Equalization. A Fluctuating Charge Model with Correct Asymptotics. *Chem. Phys. Lett.* **2007**, *438*, 315−320.
(54) Lii, J. H.; Allinger, N. L. Molecular Mechanics. The MM3 Force Field for Hydrocarbons. 2. Vibrational Frequencies and Thermodynamics. *J. Am. Chem. Soc.* **1989**, *111*, 8566−8575.
(55) Verstraelen, T.; Vanduyfhuys, L.; Vandenbrande, S.; Rogge, S. M. J. Yaff, yet Another Force Field, http://molmod.ugent.be/software/ (accessed September 12, 2020).
(56) Rogge, S. M. J.; Vanduyfhuys, L.; Ghysels, A.; Waroquier, M.; Verstraelen, T.; Maurin, G.; Van Speybroeck, V. A Comparison of Barostats for the Mechanical Characterization of Metal−Organic Frameworks. *J. Chem. Theory Comput.* **2015**, *11*, 5583−5597.
(57) Nosé, S. A Unified Formulation of the Constant Temperature Molecular Dynamics Methods. *J. Chem. Phys.* **1984**, *81*, 511−519.
(58) Hoover, W. G. Canonical Dynamics: Equilibrium Phase-Space Distributions. *Phys. Rev. A* **1985**, *31*, 1695−1697.
(59) Martyna, G. J.; Tuckerman, M. E.; Tobias, D. J.; Klein, M. L. Explicit Reversible Integrators for Extended Systems Dynamics. *Mol. Phys.* **1996**, *87*, 1117−1157.
(60) Savitzky, A.; Golay, M. J. E. Smoothing and Differentiation of Data by Simplified Least Squares Procedures. *Anal. Chem.* **1964**, *36*, 1627−1639.
(61) Barthelet, K.; Marrot, J.; Riou, D.; Férey, G. A Breathing Hybrid Organic−Inorganic Solid with Very Large Pores and High Magnetic Characteristics. *Angew. Chem., Int. Ed.* **2002**, *41*, 281.
(62) Loiseau, T.; Serre, C.; Huguenard, C.; Fink, G.; Taulelle, F.; Henry, M.; Bataille, T.; Férey, G. A Rationale for the Large Breathing of the Porous Aluminum Terephthalate (MIL-53) Upon Hydration. *Chem. − Eur. J.* **2004**, *10*, 1373−1382.
(63) Wentz, H. C.; Skorupskii, G.; Bonfim, A. B.; Mancuso, J. L.; Hendon, C. H.; Oriel, E. H.; Sazama, G. T.; Campbell, M. G. Switchable Electrical Conductivity in a Three-Dimensional Metal−Organic Framework via Reversible Ligand n-Doping. *Chem. Sci.* **2020**, *11*, 1342−1346.
(64) Garai, B.; Mallick, A.; Banerjee, R. Photochromic Metal−Organic Frameworks for Inkless and Erasable Printing. *Chem. Sci.* **2016**, *7*, 2195−2200.
(65) Xie, Y.-X.; Zhao, W.-N.; Li, G.-C.; Liu, P.-F.; Han, L. A Naphthalenediimide-Based Metal−Organic Framework and Thin Film Exhibiting Photochromic and Electrochromic Properties. *Inorg. Chem.* **2016**, *55*, 549−551.
(66) Guo, Z.; Panda, D. K.; Maity, K.; Lindsey, D.; Parker, T. G.; Albrecht-Schmitt, T. E.; Barreda-Esparza, J. L.; Xiong, P.; Zhou, W.; Saha, S. Modulating the Electrical Conductivity of Metal-Organic Framework Films with Intercalated Guest π-Systems. *J. Mater. Chem. C* **2016**, *4*, 894−899.
(67) Guo, Z.; Panda, D. K.; Gordillo, M. A.; Khatun, A.; Wu, H.; Zhou, W.; Saha, S. Lowering Band Gap of an Electroactive Metal-Organic Framework via Complementary Guest Intercalation. *ACS Appl. Mater. Interfaces* **2017**, *9*, 32413−32417.
(68) Castaldelli, E.; Imalka Jayawardena, K. D. G.; Cox, D. C.; Clarkson, G. J.; Walton, R. I.; Le-Quang, L.; Chauvin, J.; Silva, S. R. P.; Demets, G. J.-F. Electrical Semiconduction Modulated by Light in a Cobalt and Naphthalene Diimide Metal−Organic Framework. *Nat. Commun.* **2017**, *8*, 2139.
(69) Zhou, W.; Yildirim, T. Lattice Dynamics of Metal−Organic Frameworks: Neutron Inelastic Scattering and First-Principles Calculations. *Phys. Rev. B* **2006**, *74*, No. 180301.
(70) Rogge, S. M. J.; Wieme, J.; Vanduyfhuys, L.; Vandenbrande, S.; Maurin, G.; Verstraelen, T.; Waroquier, M.; Van Speybroeck, V. Thermodynamic Insight in the High-Pressure Behavior of UiO-66: Effect of Linker Defects and Linker Expansion. *Chem. Mater.* **2016**, *28*, 5721−5732.

https://doi.org/10.1021/acs.chemmater.1c03236
Chem. Mater. XXXX, XXX, XXX−XXX

(71) Boyd, P. G.; Moosavi, S. M.; Witman, M.; Smit, B. Force-Field Prediction of Materials Properties in Metal−Organic Frameworks. *J. Phys. Chem. Lett.* **2017**, *8*, 357−363.
(72) Rogge, S. M. J.; Waroquier, M.; Van Speybroeck, V. Reliably Modeling the Mechanical Stability of Rigid and Flexible Metal−Organic Frameworks. *Acc. Chem. Res.* **2018**, *51*, 138−148.
(73) Wieme, J.; Vanduyfhuys, L.; Rogge, S. M. J.; Waroquier, M.; Van Speybroeck, V. Exploring the Flexibility of MIL-47(V)-Type Materials Using Force Field Molecular Dynamics Simulations. *J. Phys. Chem. C* **2016**, *120*, 14934−14947.
(74) Hoffmann, R. How Chemistry and Physics Meet in the Solid State. *Angew. Chem., Int. Ed.* **1987**, *26*, 846−878.
(75) Foster, M. E.; Sohlberg, K.; Spataru, C. D.; Allendorf, M. D. Proposed Modification of the Graphene Analogue $Ni_3(HITP)_2$ to Yield a Semiconducting Material. *J. Phys. Chem. C* **2016**, *120*, 15001−15008.
(76) Dong, R.; Han, P.; Arora, H.; Ballabio, M.; Karakus, M.; Zhang, Z.; Shekhar, C.; Adler, P.; Petkov, P. S.; Erbe, A.; Mannsfeld, S. C. B.; Felser, C.; Heine, T.; Bonn, M.; Feng, X.; Cánovas, E. High-Mobility Band-like Charge Transport in a Semiconducting Two-Dimensional Metal−Organic Framework. *Nat. Mater.* **2018**, *17*, 1027−1032.
(77) Chen, L.; Mowat, J. P. S.; Fairen-Jimenez, D.; Morrison, C. A.; Thompson, S. P.; Wright, P. A.; Düren, T. Elucidating the Breathing of the Metal−Organic Framework MIL-53(Sc) with Ab Initio Molecular Dynamics Simulations and in Situ X-Ray Powder Diffraction Experiments. *J. Am. Chem. Soc.* **2013**, *135*, 15763−15773.
(78) Reinsch, H.; Pillai, R. S.; Siegel, R.; Senker, J.; Lieb, A.; Maurin, G.; Stock, N. Structure and Properties of Al-MIL-53-ADP, a Breathing MOF Based on the Aliphatic Linker Molecule Adipic Acid. *Dalton Trans.* **2016**, *45*, 4179−4186.
(79) Wieme, J.; Rogge, S. M. J.; Yot, P. G.; Vanduyfhuys, L.; Lee, S. K.; Chang, J. S.; Waroquier, M.; Maurin, G.; Van Speybroeck, V. Pillared-Layered Metal−Organic Frameworks for Mechanical Energy Storage Applications. *J. Mater. Chem. A* **2019**, *7*, 22663−22674.
(80) Yang, X.; Si, L.; Xie, G.; Zhang, L.; Guo, D.; Luo, J. Intrinsic Adsorption Behaviour Related to the Structural and Mechanical Properties of Flexible Metal−Organic Frameworks Co(bdp). *Comput. Mater. Sci.* **2020**, *177*, No. 109543.

https://doi.org/10.1021/acs.chemmater.1c03236
Chem. Mater. XXXX, XXX, XXX−XXX